Research Paper

Analytical estimation of fusion zone dimensions and cooling rates in part scale laser powder bed fusion

P. Zagade [a,b], B.P. Gautham [a], A. De [*,b], T. DebRoy [c]

[a] *TCS Research, Tata Consultancy Services, Pune, India*
[b] *Indian Institute of Technology Bombay, India*
[c] *The Pennsylvania State University, USA*

ABSTRACT

The laser powder bed fusion process is increasingly used for the building of metallic parts by melting and solidification of alloy powders under a fast-moving finely focussed laser beam. A quick estimation of the resulting temperature field, fusion zone dimensions, and cooling rates is needed to ensure the manufacture of dimensionally accurate parts with minimum defects. A novel three-dimensional analytical heat transfer model with a volumetric heat source that can simulate the laser powder bed fusion process in part scale quickly and reliably is proposed here. The volumetric heat source term is constructed to analytically simulate the evolution of melt pools with a fair range of depth to width ratio. The proposed analytical model can simulate the building of multiple tracks and layers in part scale dimensions significantly faster than all the numerical models reported in the literature. The computed results of fusion zone shapes and sizes and cooling rates are found to be in good agreement with the experimentally reported results in builds of three commonly used alloys with diverse materials properties, SS316L, Ti6Al4V, and AlSi10Mg. Based on the analytically computed results, a set of easy-to-use process maps is presented to estimate multiple process conditions to obtain a set of target fusion zone dimensions without trial-and-error testing.

1. Introduction

The laser powder bed fusion (LPBF) process builds three-dimensional parts by melting and solidification of alloy powders along multiple tracks and layers guided by a computer [1,2]. A prior estimation of the temperature field and fusion zone dimensions during the LPBF process is a necessity to reduce the volume of trial-and-error experiments to obtain parts with minimum defects [1,3]. Computer-based numerical models have emerged as potential tools but these models are time intensive and their applications have been limited mostly to a single track of deposit rather than real parts [4–6] because numerical methods require very fine discretization in space and time [4]. As a result, the simulation of the overall part dimensions involves thousands of tracks and layers and requires enormous computational time and storage [4]. For example, the simulation of a cubic centimeter of deposit typically requires computational times ranging from a few weeks to several years depending on the type of numerical calculations [4]. What is needed is an analytical model that is computationally efficient, rigorously tested in part scale, and can operate in inexpensive computers, thus expanding

the reach of the computational heat transfer in practical additive manufacturing applications.

The numerical heat transfer and fluid flow models have offered reliable estimations of fusion pool dimensions [5,7], cooling rates [6], and the susceptibility of defects [8–11] for LPBF of commonly used powder alloys. Heat conduction models neglect the convective transport of heat in the melt pool [12,13]. As the mixing of hot and cold liquid is neglected, the heat conduction models predicted higher peak temperature [6,11], narrower and shallower melt pool [11], and higher cooling rates [14]. The numerical heat transfer and fluid flow models require huge computational memory and time and could simulate part dimensions only up to a few tens of millimeters [6,15–17].

The analytical heat transfer models have been used to predict the temperature field, fusion zone dimensions, and cooling rates for fusion welding processes [18–21], which have some similarities with the LPBF process [22,23]. Unlike in fusion welding, the LPBF process involves rapid heating of the powder particles with a fast-moving finely focussed laser spot creating tiny fusion zones, which is quickly solidified [1]. The LPBF process is characterized by smaller dimensions of the fusion zone

in comparison with the directed energy deposition (DED) processes. As a result, the Peclet number (Pe), which is the ratio of the heat transported by convection to the heat transported by conduction is much smaller for the LPBF process than the other additive manufacturing (AM) processes [24]. The low values of Pe in LPBF and the small size of fusion zone enable analytical heat conduction calculations with good accuracy in part scale. However, the development and use of comprehensive analytical models to simulate typical three-dimensional multi-track multi-layer deposits in part scale are just beginning [25–29].

Here we develop an analytical heat conduction model for the estimation of temperature field, fusion zone dimensions, and cooling rates for LPBF of multiple tracks and layers quickly and reliably. A volumetric heat source term is developed and integrated with the analytical thermal model to improve the estimation of the fusion zone dimensions, temperature fields, and cooling rates. The analytically calculated fusion zone dimensions and cooling rates are compared with the independent experimental results for LPBF of three commonly used alloys e.g. Ti6Al4V, SS316L, and AlSi10Mg. Next, a set of easy-to-use maps that demonstrate the computed fusion zone geometry for various combinations of laser power and scanning speed are presented for LPBF of these three alloys. Finally, the computational time to simulate a typical part scale deposition volume of ten cubic centimeters by the proposed analytical model is compared with the various numerical models reported in the literature.

2. Analytical heat transfer model

Fig. 1(a) shows a schematic diagram of the solution domain with multiple tracks and layers on a substrate plate. The scanning and hatching directions are considered to be in the XY-plane, while the deposited layers move up in the positive Z-direction. The distance between the two adjacent tracks is referred to as the hatch spacing as shown schematically in Fig. 1(b). The three-dimensional transient heat conduction equation and the associated boundary conditions are solved analytically with a specially defined volumetric heat source term to analyze the LBPF process. The key assumptions to develop the analytical heat transfer model, the governing equations and the boundary conditions and the volumetric heat source term are presented in detail in the following section.

2.1. Assumptions

The size of the substrate in the LPBF process is usually several hundred times larger in comparison to the focussed laser beam diameter and the melt pool dimensions. Hence, the solution domain including the substrate and the powder mass is considered semi-infinite [25]. The laser beam energy melts the powder alloy and creates a tiny melt pool

Fig. 1. Schematic presentation of (a) three-dimensional solution domain and (b) hatch spacing considered to simulate laser powder bed fusion process.

with little loss of alloying elements due to vaporization [1]. The melt pool cools rapidly to create the solidified tracks as the laser beam moves with a high scanning speed [1]. The net effect of the latent heat during the transformation of the state of powder materials on the overall temperature field is therefore assumed to be negligible. Hence, the latent heat of melting and solidification is ignored, which is expected to result in little inaccuracy in the estimation of the mushy region.

The effect of convective transport of heat inside the melt pools is also neglected considering the small size and fast freezing nature of the pools. The error due to the neglect of the convective transport of heat in a melt pool can be examined by estimating the Peclet number, uL/α, where u is the local flow velocity, L is the characteristic length, and α is the thermal diffusivity of the material. The average convective velocity within a melt pool in LPBF processes is reported in the range of 0.1–0.7 m/s and the characteristic length L can be considered equal to the focussed beam radius [9,11]. The expected values of the Peclet number in the melt pool would therefore be less than unity for commonly used powder alloys and process conditions in LPBF. Therefore, the role of convection in LPBF process is significantly less important than in fusion welding and directed energy deposition (DED) based AM processes.

2.2. Governing equations and boundary conditions

The energy supplied through the laser beam is absorbed by the powder particles and conducted through the surrounding powder bed, solidified layers underneath, and the substrate plate, which is analyzed following the governing equation as [30]:

$$k\left(\frac{\partial^2 T}{\partial x^2} + \frac{\partial^2 T}{\partial y^2} + \frac{\partial^2 T}{\partial z^2}\right) + \dot{Q} = \rho C \frac{\partial T}{\partial t} \tag{1}$$

where k, ρ, C, T, and t are the thermal conductivity, density, specific heat, and temperature and time variables, respectively. The term $\dot{Q}$ accounts for the rate of heat input per unit volume and is expressed in terms of fixed coordinate and time. The corresponding boundary conditions considering the solution domain including the substrate and the powder mass to be semi-infinite is written as:

$$(T - T_0) = 0 \text{ at } (x \to \pm\infty, y \to \pm\infty, z \to -\infty) \tag{2}$$

where T_0 is the initial or ambient temperature and presumed to be 300 K. The heat loss due to radiation and convection from the top surface is assumed to be negligible, and expressed as

$$\frac{\partial T}{\partial z} = 0 \text{ at } z = 0 \tag{3}$$

Furthermore, the initial condition for the governing equation is considered as

$$T(x, y, z, t) = T_0 \text{ at } t = 0 \tag{4}$$

2.3. Volumetric heat source

The laser beam penetrates through a powder layer thereby heating the particles that can absorb energy through multiple reflections of the beam [1,31]. The extent of the energy absorbed by the powder alloy and the substrate will primarily be governed by the beam size, the nature of the distribution of the beam energy, and the mode of melting. A volumetric heat source term is therefore considered to account for the absorption of beam energy by the powder alloy and the substrate as [32].

$$\dot{Q}(x, y, z, t) = \frac{f_p \eta P}{\pi r_b^2} \exp\left\{ -\frac{f_p(x')^2 + f_p(y')^2}{r_b^2} \right\} \times \frac{\sqrt{f_d}}{h\sqrt{\pi}} \exp\left(-\frac{f_d z^2}{h^2} \right) \tag{5}$$

where P is the laser power, η is the absorption coefficient of powder particles, r_b is the beam radius, f_p and f_d are the distribution factors for the laser beam intensity in the planar and Z-directions, respectively and
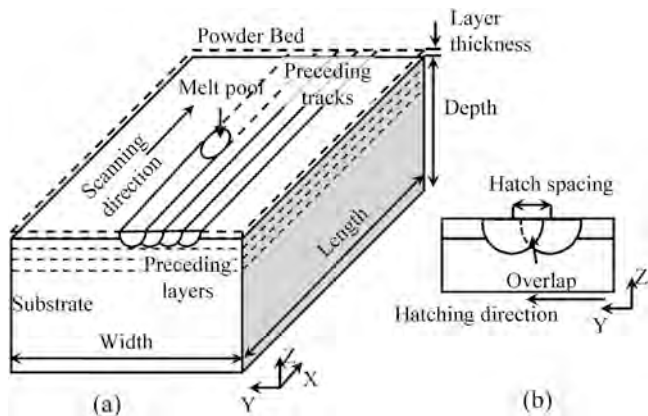
h is the height of the volumetric source and,

$$x' = x - (x_s + v_x t) \tag{6}$$

$$y' = y - (y_s + v_y t) \tag{7}$$

where t is the time since the start of the traveling of the laser beam from the point (x_s, y_s, z_s) at constant linear speeds of v_x and v_y in X and Y directions, respectively.

The parameter h in Eq. (5) depicts the extent of the introduction of the heat source in the Z-direction and is construed to be equivalent to the depth of the melt pool. In order to estimate h for input to the analytical model, it is considered to be a function of the absorbed laser beam energy (ΔH) and the enthalpy (h_S) at melting of the powder alloy. The term h is considered in a non-dimensional form as (h/r_b) and referred to as normalized track depth. For the laser beam scanning over a distance equal to its radius r_b with a speed v in time (r_b/v), the absorbed laser beam energy (ΔH) per unit volume, in which it is distributed, is considered as [33].

$$\Delta H = \frac{\eta P(r_b/v)}{\pi r_b^2 \sqrt{\alpha(r_b/v)}} \tag{8}$$

where α is the thermal diffusivity of the material. The enthalpy (h_S) at the melting of the powder alloy is estimated as a product of its density (ρ), specific heat (C), and solidus temperature (T_S). The normalized track depth (h/r_b) is thereafter expressed as a function of the ratio ($\Delta H/h_S$), which is referred to as normalized energy input, as

$$\frac{h}{r_b} = 0.08 \left(\frac{\eta P(r_b/v)}{\pi r_b^2 \sqrt{\alpha(r_b/v)}} \times \frac{1}{\rho C T_s} \right)^{1.4} \tag{9}$$

The fitting constants, 0.08 and 1.4 in Eq. (9) are determined using the least square method by considering a range of experimentally observed melt pool depths as equal to h for LPBF of three commonly used powder alloys Ti6Al4V [25,34–37], SS316 [38–40], and AlSi10Mg [41]. Table 1 presents the process conditions and Table 2 shows the material properties that are considered to derive the fitting constant in Eq. (9).

Fig. 2 shows the normalized track depth (h/r_b) as a function of the normalized energy input ($\Delta H/h_S$) for LPBF of three powder alloys considering the values of h equal to the melt pool depth, observed experimentally from the reported literature and estimated using Eq. (9). At lower energy input, the conduction mode of melting prevails resulting in shallower melt pools and smaller values of (h/r_b). In contrast, an increase in energy input results in keyhole mode of melting and deep melt pool leading to the higher values of (h/r_b) [33]. Overall, Fig. 2 shows a good agreement for the fitted relation in Eq. (9), which is therefore used to estimate h for an input to the volumetric heat source term, Eq. (5), for analytical estimation of the temperature field.

3. Analytical solutions

The development of the analytical solution for the governing equation, Eq. (1) along with the corresponding necessary conditions, Eqs. (2)–(4) and the volumetric heat source term, Eq. (5) is presented in this

Table 1
Process conditions used for Eq. (9).

Parameter	Ti6Al4V [25,34–37]	SS316L [38–40]	AlSi10Mg [41]
Laser power, P (W)	50–520	75–500	150–350
Scanning speed, v (m/s)	0.20–1.86	0.1–2.0	0.2–2.4
Laser beam radius, r_b, (µm)	27–70	27–35	35
Beam distribution parameters, f_p, f_d	1.0, 2.0	1.0, 2.0	1.0, 2.0
Melt pool depth, d (mm)	0.006–0.443	0.014–0.597	0.095–0.490
Layer height of tracks, (mm)	0.03–0.05	0.030–0.075	0.030
Absorption coefficient, η	0.60	0.60	0.50

Table 2
Material properties used for Eq. (9) [42].

Parameter	Ti6Al4V	SS316L	AlSi10Mg
Density, ρ (kg m^{-3})	4200	7400	2610
Solidus temperature, T_S (K)	1878	1658	823
Specific heat, C (J kg^{-1} K^{-1})	830	716	1160
Diffusivity, α (m²/s)	8.06e-6	5.58e-6	44.5e-6

Properties are considered at the solidus temperature of powder alloy
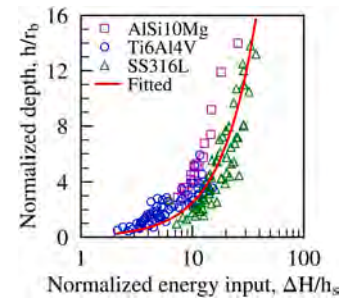
Fig. 2. Variation of normalized pool depth (h/r_b) as a function of normalized energy input ($\Delta H/h_S$). The scattered points are plotted considering h as the experimentally observed melt pool depths from independent literature - Ti6Al4V [25,34–37], SS316 [38–40] and AlSi10Mg [41]. The fitted line is plotted with the value of h estimated from Eq. (9).

section for laser beam scanning of single and multiple linear tracks.

3.1. Material properties

During the LPBF process, the powder alloy and the solid material undergo repeated cycles of melting and solidification and the physical properties of the material at different locations would vary depending on its state and the temperature. It is quite challenging to derive an analytical solution of the governing equation considering the alloy material properties as a function of its state and temperature. A simple and tractable framework is therefore proposed to consider the thermal conductivity and specific heat as a linear function of temperature. Furthermore, the layer thickness in the LPBF process is usually small (0.03–0.05 mm) compared with the substrate thickness (few tens of millimeters). The heat dissipation through the substrate is therefore expected to be predominant and the analytical calculations are conducted using the properties of the substrate. An effective heat capacity is considered for the locations exceeding boiling temperature by using an elevated value of the specific heat to account for the latent heat of evaporation [43]. Table 3 lists the thermo-physical properties of

Table 3
Material properties for Ti6Al4V, SS316L and AlSi10Mg [42,44].

	Ti6Al4V	SS316L	AlSi10Mg
Density, ρ (kg m^{-3})	4200	7400	2610
Solidus (T_S), liquidus (T_L), & boiling (T_B) temperatures, (K)	1878, 1923, 3315	1658, 1723, 3100	823, 850, 2793
Heat of evaporation, L_e (J kg^{-1})	8.89×10^6	6.08×10^6	10.78×10^6
Conductivity, k (W m^{-1} K^{-1})	8.7 $(1 + 1.18 \times 10^{-3} \times T)$	11.3 $(1 + 0.89 \times 10^{-3} \times T)$	118 $(1 + 0.10 \times 10^{-3} \times T)$
Specific heat, C (J kg^{-1} K^{-1})	260 $(1 + 1.18 \times 10^{-3} \times T)$	280 $(1 + 0.89 \times 10^{-3} \times T)$	980 $(1 + 0.10 \times 10^{-3} \times T)$

Ti6Al4V, SS316, and AlSi10Mg alloys that are considered in the present analysis.

3.2. Solution scheme for single track

An analytical solution of Eq. (1) considering the initial and boundary conditions Eqs. (2)–(4) and, a volumetric heat source (Eq. (5)) moving along a single linear track in the XY plane is developed using Green's function [30,32,45] as:

3.3. Solution scheme for multiple tracks

Fig. 3(a) shows schematically the movement of the laser beam along multiple linear connected tracks where the arrows indicate the scanning direction of the beam along a track. The total scanned path at any time instance t is considered to compose of the previously scanned n_p number of tracks and the track being scanned, which is referred to as the current track. Any previously laid i^{th} track is designated by the starting location (x_s^i, y_s^i), the starting time t_s^i, the ending time t_e^i and, the scanning speeds v_x^i and v_y^i respectively in X and Y directions as shown in Fig. 3(b). The

$$T(x, y, z, t) = \frac{1}{m} \times \left[\left(2m \int_{t'=0}^{t'=t} \frac{2f_p \eta P \sqrt{f_d}}{\rho C_0 \pi \sqrt{\pi}} \frac{1}{\tau''} \exp\left\{ -\frac{f_p\{(x')^2 + (y')^2\}}{4f_p \alpha t'' + r_b^2} - \frac{f_d(z)^2}{4f_d \alpha t'' + h^2} \right\} dt' + (1 + mT_0)^2 \right)^{\frac{1}{2}} - 1 \right] \tag{10}$$

$$T(x, y, z, t) = \frac{1}{m} \left[\left\{ \frac{4m\eta P f_p \sqrt{f_d}}{\rho C_0 \pi \sqrt{\pi}} \left(\int_{t'=t_s^f}^{t'=t} \frac{1}{\tau''} \exp\left[-\frac{f_p\left\{ \left(x_f''\right)^2 + \left(y_f''\right)^2 \right\}}{4f_p \alpha t'' + r_b^2} - \frac{f_d(z)^2}{4f_d \alpha t'' + h^2} \right] dt' \right. \right. \tag{15}$$

$$\left. \left. + \sum_{i=1}^{i=n_p} \int_{t'=t_s^i}^{t'=t_e^i} \frac{1}{\tau''} \exp\left[-\frac{f_p\left\{ \left(x_i''\right)^2 + \left(y_i''\right)^2 \right\}}{4f_p \alpha t'' + r_b^2} - \frac{f_d(z)^2}{4f_d \alpha t'' + h^2} \right] dt' \right) + (1 + mT_0)^2 \right\}^{\frac{1}{2}} - 1 \right]$$

where t' is the integration variable for time and t is the time instance at which the solution will be evaluated. The thermal conductivity k and specific heat C are considered to be a linear function of temperature (T) as $k = k_0(1 + mT)$ and $C = C_0(1 + mT)$, where m, k_0, and C_0 are materials constants. Other variables in Eq. (10) are expressed as,

$$t'' = (t - t') \tag{11}$$

$$\tau'' = \left(4f_p \alpha t'' + r_b^2\right)\sqrt{4f_d \alpha t'' + h^2} \tag{12}$$

$$x'' = \{x - (x_s + v_x t')\} \tag{13}$$

$$y'' = \{y - (y_s + v_y t')\} \tag{14}$$

Further detailed derivation of Eq. (10) is presented in Appendix-I. An enhancement of Eq. (10) to simulate the scanning of laser beam along multiple tracks is presented in the following section.
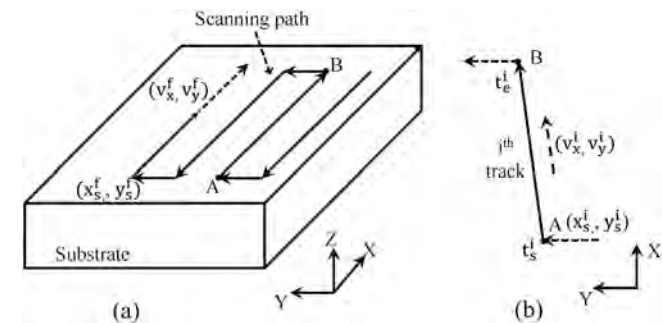
current scanning track is designated with the starting location and time as (x_s^f, y_s^f) and t_s^f, respectively, and the scanning speeds v_x^f and v_y^f in X and Y directions. The analytical solution of temperature field while scanning through multiple linear connected tracks is developed using superposition principle by summing up the contributions of heat input in the current and all the previously scanned tracks and expressed as:

where

$$x_f'' = x - \left\{ x_s^f + v_x^f(t' - t_s^f) \right\} \tag{16}$$

$$y_f'' = y - \left\{ y_s^f + v_y^f(t' - t_s^f) \right\} \tag{17}$$

$$x_i'' = x - \left\{ x_s^i + v_x^i(t' - t_s^i) \right\} \tag{18}$$

Fig. 3. Schematic presentation of (a) movement of laser beam along planar tracks, and (b) nomenclature associated with a typical i^{th} track.
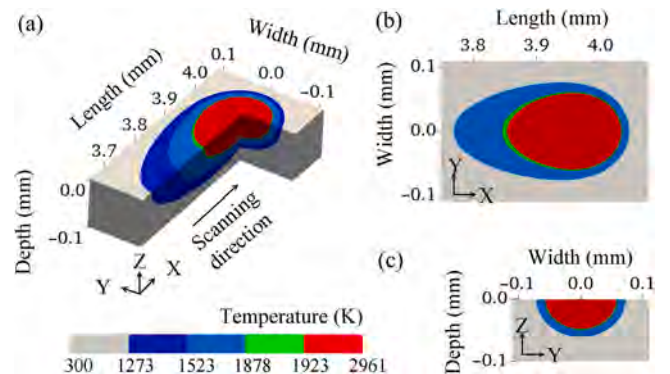

Fig. 4. Analytically calculated temperature profile for single-track deposition of Ti6Al4V powder for a laser beam power of 60 W, beam radius of 0.05 mm and scanning speed of 0.5 m/s - (a) three-dimensional isometric view, (b) top view (YX), and (c) transverse cross-sectional view (YZ).

$$y_i'' = y - \left\{ y_s^i + v_y^i (t' - t_s^i) \right\} \tag{19}$$

Eq. (15) is used to estimate the temperature field for the deposition of multiple linear tracks on a layer. To compute the temperature field for deposition in subsequent upper layers, the frame of reference is shifted up in the Z-direction by a distance equal to the layer thickness, and Eq. (15) is employed once again with all the in-layer variables redefined for the new layer and Z = 0 matching with its top surface.

At first, efforts are undertaken to estimate the melt pool dimensions for deposition of Ti6Al4V, SS316L, and AlSi10Mg alloy powders based on the analytically computed temperature field for a range of process conditions as mentioned in Table 1. The analytically computed melt pool dimensions are examined against both the experimentally observed and the numerically computed results from the independent literature.

4. Model testing and validation

4.1. Fusion zone geometry

Fig. 4 presents the analytically computed temperature field in three-dimension and across different two-dimensional cross-sections for deposition of Ti6Al4V powder along a single track for a laser power of 60 W and a scanning speed of 0.5 m/s. The fusion zone or the melt pool is designated by the region encompassed by the liquidus temperature isotherm, 1923 K. The region between the liquidus and solidus temperature, 1878 K, represents the mushy zone and is shown with green color. The estimated peak temperature tends to be slightly higher near the center of the heat source, which is attributed to the typical nature of the analytical solution and considered as an artifact [18]. A more realistic estimation of the peak temperature warrants the consideration of the convective transport of heat within the melt pool [14]. The length, width and depth of the melt pool, i.e. the region enclosed by the liquidus temperature isotherm, 1923 K in Fig. 4(a-c), equal to around 0.18, 0.12, and 0.05 mm, respectively.

Fig. 5 shows the analytically calculated temperature field in three-dimension (Fig. 5a), and across different two-dimensional cross-sections (Fig. 5b-c), for deposition of a single track with SS316L powder at a laser power of 60 W and scanning speed of 0.5 m/s. The melt pool length, width, and depth are determined by considering the region enclosed by the liquidus temperature isotherm, 1723 K, as 0.19, 0.11, and 0.04 mm, respectively. A comparison of Figs. (4–5) shows slightly larger melt pool volumes for Ti6Al4V alloy, which is attributed to its smaller density and higher thermal diffusivity compared to that for SS316L.

Fig. 6 shows a comparison of the transverse cross-sections of the computed melt pool and the corresponding deposited tracks [34] for Ti6Al4V powder at a constant scanning speed and three different laser powers. At a smaller laser power of 100 W, both the deposited track and the calculated melt pool cross-sections exhibit a near semi-circular shape with the depth of the track approximately equaling to its half-width, as shown in Fig. 6(a, d). With the increase in the laser power to 150 and 195 W, the track depths exhibit a steeper increase in comparison to the corresponding track widths in Fig. 6(b, e) and Fig. 6(c, f). The difference between the calculated melt pool shapes and the corresponding deposited track profiles tends to rise at higher laser power. At lower laser powers, the deposited track cross-sections indicate a conduction mode of melting. The mode shifts towards the keyhole mode of melting as the laser power is increased [34]. As a result, the analytically calculated melt pool shapes at higher laser power show more discrepancy, around 15–18%, in comparison to the corresponding measured track dimensions [34].

Fig. 7 shows a comparison of the computed melt pool shapes and the corresponding experimentally observed cross-sections of deposited tracks of SS316L powder [40] at a constant laser power and two different scanning speeds. Both Fig. 7(a, c) and Fig. 7(b, d) show that the calculated melt pool depths and experimentally deposited track depths reduce with an increase in the scanning speed while the width remains nearly unaffected. An increase in the scanning speed results in a decrease in the heat input per unit length of deposit leading to a smaller depth of the melt pool and the deposited track. Both Figs. (6,7) show a fair agreement between the analytically calculated melt pool profiles and the corresponding deposited track shapes for several process conditions. Figs. (6,7) also manifest that the analytical model calculations can undertake the effect of the thermophysical properties of the respective powder alloys. For example, a higher thermal diffusivity and smaller density of Ti6Al4V powders resulted in greater melt pool depths in comparison to that for SS316L powders.

Figs. (6–7) show a fair agreement between the calculated melt pool dimensions and the corresponding experimentally observed profiles of the single track deposits for two commonly used powder alloys. Eq. (15) is subsequently used to estimate the melt pool dimensions for the deposition of multiple tracks. Fig. 8 shows a comparison of the analytically calculated pool shapes and the corresponding experimentally observed [35] cross-section of a multi-track deposit of Ti6Al4V alloy powder. A slow increase in the depth of the melt pool and the deposited tracks is noted as the number of tracks increases, which is attributed to the augmented resident temperature of the overall build as more and more tracks are laid. The analytically calculated melt pool profiles depict a fair match with that of the corresponding experimentally observed tracks with a discrepancy of around 5%.

Fig. 9 shows a comparison between the size and shapes of the analytically calculated melt pool and the corresponding experimentally observed [46] tracks for a two-track deposit with SS316L alloy powder. The overall discrepancy between the calculated and the corresponding measured dimensions from independent literature [46] lies in the range of 15–20%. Overall, Figs. (8–9) show that the developed analytical model can provide practically usable estimates of the deposited track dimensions for LPBF of commonly used powder alloys with diverse thermophysical properties in single and multiple track configurations.

Amongst several underlying simplifications that are required to find a tractable form of the analytical model, the need to consider a semi-infinite solution domain for the substrate and alloy powders is a major constraint. In contrast to the analytical solution, numerical heat conduction models based on the finite element method (FEM) or finite volume method (FVM) are capable of considering actual substrate and track geometries. As a result, such models can aim at simulating the LPBF process as they occur in real-time although at a cost of huge computational demand. It is therefore prudent to examine the consistency of the analytically calculated results presented in this work with similar ones reported by well-established numerical process models.

Fig. 10 shows a comparison of the analytically calculated melt pool dimensions with that reported from a FEM-based numerical model [17] for LPBF of SS316L powder at different laser powers and scanning
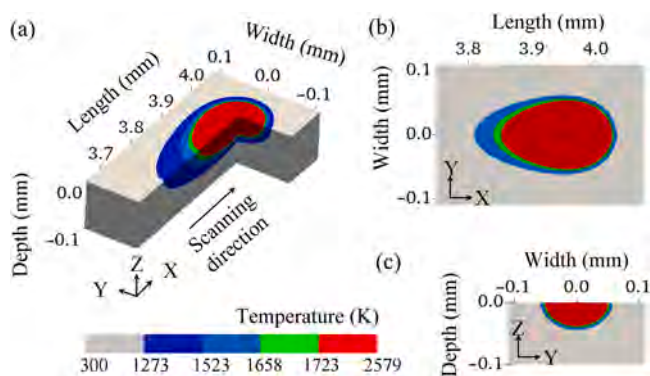

Fig. 5. Analytically calculated temperature profile for single-track deposition of SS316L powder for a laser beam power of 60 W, beam radius of 0.05 mm and scanning speed of 0.5 m/s - (a) three-dimensional isometric view, (b) top view (YX), and (c) transverse cross-sectional view (YZ).
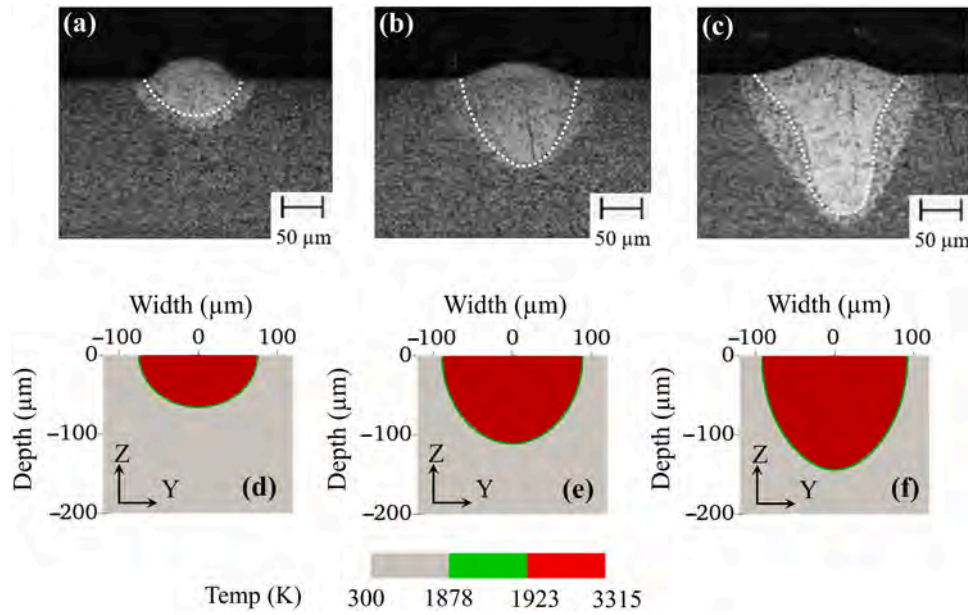
Fig. 6. Experimentally observed (a, b, c) [34] and the corresponding analytically calculated (d, e, f) transverse cross-sectional view (YZ) for single-track deposition of Ti6Al4V powder for a laser scanning speed of 0.5 m/s and beam radius of 0.05 mm, and different beam powers of (a, d) 100 W, (b, e) 150 W, and (c, f) 195 W. Fusion zone boundaries are added on the micrographs (a-c) following the reported track dimensions in reference [34].
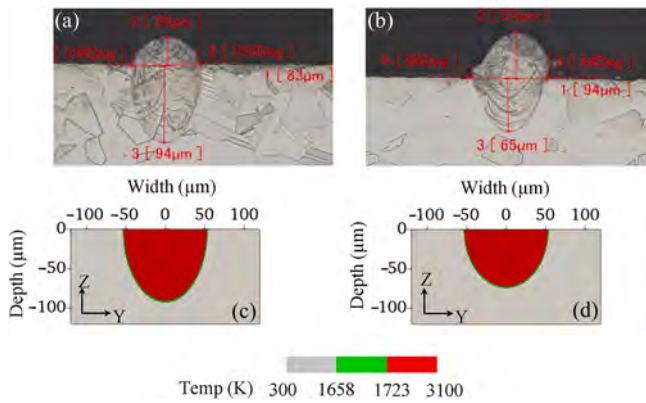

Fig. 7. Experimentally observed (a, b) [40] and the corresponding analytically calculated (c, d) transverse cross-sectional view (YZ) of deposited track profiles for single-track deposition of SS316L powder for a constant laser beam power of 300 W, beam radius of 0.027 mm, and two different laser scanning speeds of (a, c) 1.5 m/s and (b, d) 1.8 m/s.

speeds. Fig. 10(a) shows that an increase in laser power results in larger melt pool dimensions, which is expected. In contrast, Fig. 10(b) shows that an increase in the scanning speed leads to an increase in the length of the melt pool while the width and depth of the pool reduce. An increase in the scanning speed reduces the heat input per unit length of deposition resulting in smaller melt pool volume. Overall, Fig. 10 shows a fair agreement between the analytically calculated melt pool dimensions and the corresponding computed results from a numerical heat transfer model for a range of laser powers and scanning speeds. A similar comparison of the analytically calculated melt pool dimensions with that reported by an FVM based numerical heat transfer and fluid flow model [6] for the same process conditions showed an overall discrepancy between 10% and 15%.

4.2. Cooling rate

The analytically computed temperature field is used next to estimate the cooling rate during solidification, which is an important
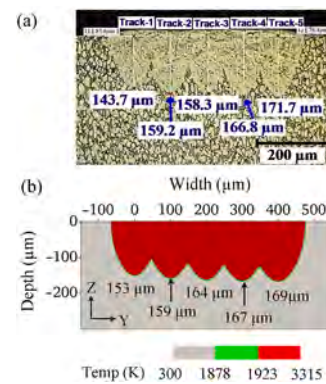

Fig. 8. Experimentally observed (a) [35] and the corresponding analytically computed (b) transverse (YZ) view of a multi-track deposit profile of Ti6Al4V powders for a laser power of 300 W, scanning speed of 1 m/s, and hatch spacing of 0.1 mm.
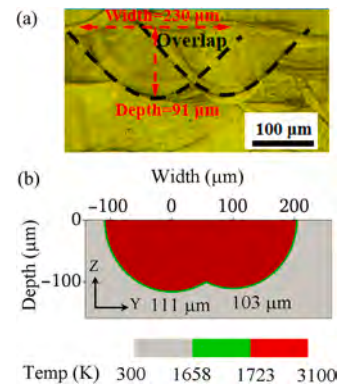

Fig. 9. Experimentally observed (a) [46] and the corresponding analytically calculated (b) transverse (YZ) cross-sectional view of deposited track profiles for a multi-track deposition with SS316L powders for a laser power of 200 W, scanning speed of 0.4 m/s, and hatch spacing of 0.1 mm [46].
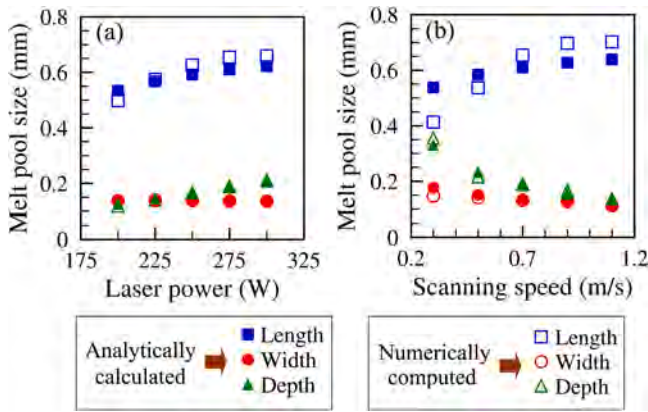
Fig. 10. Comparison of analytically calculated and corresponding numerically computed melt pool dimensions as a function of (a) laser power and (b) scanning speed for LPBF deposition of the second track along the first layer with SS316L powder. The numerically computed values are obtained from a FEM-based heat conduction analysis [17].
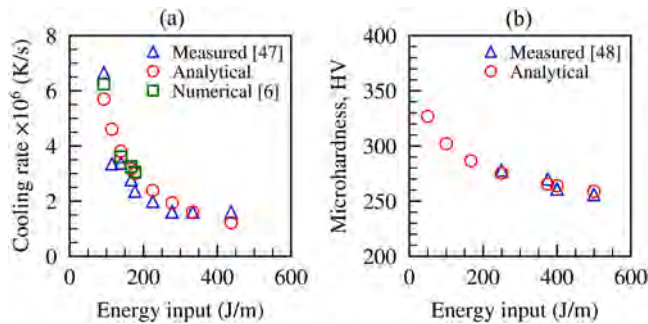

Fig. 11. Comparison of (a) analytically calculated and, corresponding numerically computed [6] and experimentally measured [47] cooling rates, and, (b) analytically estimated and corresponding experimentally measured [48] microhardness as a function of energy input per unit length for single track depositions with SS316 alloy powder. The numerically computed cooling rate values are from an FVM based heat transfer and fluid flow model as reported in [6] for a single track build with SS316L powder.

metallurgical variable to gauge the structure and property of the build for LPBF depositions. A simplified expression to estimate the cooling rate at any location, trailing to the laser beam and on the surface of a single linear track, is derived in Appendix-II. Fig. 11(a) shows a comparison of the analytically computed cooling rates with that observed experimentally [47] and computed numerically [6] as a function of heat input per unit length for deposition of single tracks with SS316L powder.
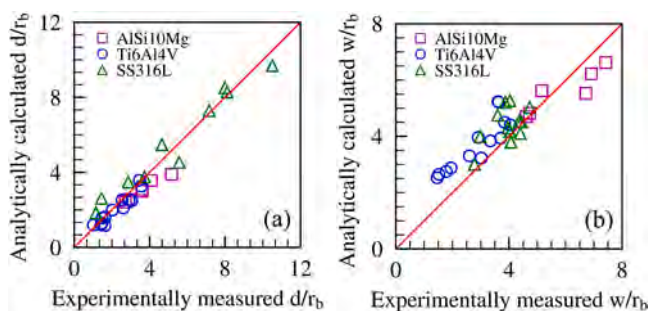
An increase in the heat input per unit length results in greater melt pool volume and reduced cooling rates as shown in Fig. 11(a). Overall, the analytically computed values of cooling rates agree well with the corresponding reported experimentally measured results [47] and that calculated from a heat transfer and fluid flow model [6] with a discrepancy of around 10–15%.

The computed cooling rates can be used further to estimate the mechanical properties such as microhardness of the solidified build using a set of constitutive relations, as shown in Appendix-II. Fig. 11(b) shows a comparison of the estimated values of microhardness with that measured and reported in independent literature for single track deposition of SS316L [48]. The decrease in hardness values with an increase in the energy input per unit length of deposition is expected as higher energy input would increase melt pool volume, reduce the cooling rate and result in coarse grain microstructure. Similar empirical constitutive relations can be pursued for other powder alloys to find out the microhardness and other properties from the analytically computed cooling rate values.

4.3. Role of different alloys

The analytical model is tested rigorously to examine its ability to account for the impact of the diverse material properties arising out of different powder alloys on the computed fusion zone dimensions for a range of LPBF process conditions. Fig. 12 shows a comparison of the analytically calculated fusion zone dimensions and the corresponding experimentally observed results from independent literature [25,34–41] for LPBF of three different alloys, e.g. Ti6Al4V, S316L and AlSi10Mg for a range of process conditions as given in Table 1. The calculated and the corresponding measured melt pool dimensions from the reported literature [25,34–41] are plotted in a dimensionless form as (d/r_b) and (w/r_b), where r_b is the laser beam radius and, w and d refer to the melt pool width and depth, respectively. Fig. 12 shows a fair match between the calculated and the measured melt pool dimensions from [25,34–41]. Overall, Fig. 12 demonstrates the applicability of the analytical model for reliable prediction of the temperature field and the fusion zone dimensions for LPBF of commonly used alloy powders and process conditions.

A guide to the selection of the key process conditions such as laser power and scanning speed, which primarily influence the melt pool dimensions, is needed to avoid multiple trial-and-error experiments while deposition of multiple tracks and layers. Fig. 13 shows the analytically computed melt pool width and depth as a function of laser beam power and scanning speed for LPBF of three commonly used powder alloys, AlSi10Mg, Ti6Al4V, and SS316L. For a constant beam power, an increase in the scanning speed reduces the melt pool dimensions, which is attributed to the decrease in available energy per unit length of deposition. In contrast, an increase in the laser power for a

Fig. 12. Analytically calculated and the corresponding experimentally observed (a) depth and (b) width of deposited tracks in normalized form for Ti6Al4V, SS316L, and AlSi10Mg powders. The measured values are taken from [25,34–37] for Ti6Al4V, [38–40] for SS316L and [41] for AlSi10Mg.
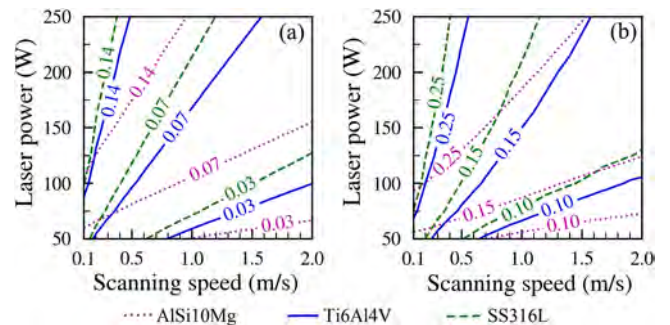

Fig. 13. Analytically computed melt pool depth (a) and width (b) as function of laser beam power and scanning speed for LPBF with AlSi10Mg, Ti6Al4V and SS316L powders. The laser beam radius is considered as 0.05 mm for all the calculations.

Table 4
Estimated computational time to simulate for LPBF processing using various approaches.

Types of model	Computational time[a] for build size (L × W × H, in mm^3)	
	(2.0 × 1.0 × 0.5)	(100 × 10 × 10)
Proposed analytical heat conduction model	48 s	44 min
FEM based heat conduction model [17]	∼ 4.5 h	∼ 1.8 × 10^3 days
FEM based heat transfer and fluid flow model [49]	∼ 5.6 h	∼ 2.3 × 10^3 days
FVM based heat transfer and fluid flow model [5]	∼ 6.6 h	∼ 2.7 × 10^3 days
FEM based heat transfer model with lumped layer approach involving multiple layers in a single one [50]	–	∼ 7.5 h
Powder scale model using discrete element method and heat and fluid flow [51]	∼ 280 h	∼ 2.4 × 10^5 days

[a] Computational times for the numerical models are assessed based on reported simulation time and build volume with the assumption of no further mesh/algorithm optimization and hardware enhancement.

constant scanning speed results in greater melt pool dimensions, which is expected. Fig. 13 indicates greater melt pool depth and width with AlSi10Mg powder in comparison to that with Ti6Al4V and SS316L powders for given laser power and scanning speed. This is attributed to the lower density and higher thermal diffusivity of AlSi10Mg powder in comparison to that for Ti6Al4V and SS316L powders. The maps like Fig. 13 can support a quick selection of the key process conditions to achieve the recommended melt pool dimensions and dimensionally consistent track profiles.

4.4. Computational time

The aforementioned discussions exhibit the strength of the proposed analytical model to compute the temperature field, melt pool dimensions, and cooling rates for LPBF of commonly used powder alloys. It is also prudent to examine the computational efficiency of the proposed analytical model in comparison to the commonly employed numerical process simulation models. Table 4 presents a comparison of the computational times to simulate the deposition of a small volume of 1 mm^3 and a typical part scale volume of 10^4 mm^3 (10 cm^3) by the proposed analytical model and various numerical models. The analytical model calculations are performed with an 11th generation core i5 notebook computer with 8 GB RAM. The computational times for the numerical models are assessed from the simulation time and the corresponding build volume as reported in the literature. The numerical models with the lumped layer approach would simulate the deposition of several layers together with a lumped heat input and hence, such models require slightly lesser computational time in comparison to the models that simulate individual tracks and layers. Overall, Table 4 shows that the analytical heat conduction model could simulate a typical part scale volume of 10^4 mm^3 (10 cm^3) in lesser than an hour. This manifests the inherent strength of the proposed analytical model as a practical tool to quickly estimate the temperature field and fusion zone dimensions for LPBF of part scale dimensions.

The aforementioned sections have illustrated that the developed analytical model can compute the fusion zone dimensions and cooling rates for LPBF of commonly used powder alloys for a wide range of process conditions at notably small computational times and with reasonable accuracy. Although early analytical models [25–29] introduced an alternate route to simulate the LPBF process, their applicability, accuracy of computed results and benchmarking for computational performances were rarely reported in the literature. These shortcomings are addressed in this paper. The primary novelty of the proposed model is the capability of predicting the melt pool geometry, temperature fields, and cooling rates rapidly and reliably in

part-scale using inexpensive computers, thus expanding the reach of simulations to practical usage by all. However, the convective transport of heat in the melt pool is neglected to keep the derivation of the analytical model tractable. This simplification can limit the application of the model to examine the role of surface-active elements [55], joint orientation effects [55], and microstructural investigations [56]. Furthermore, the assumption of semi-infinite solution domain would pose practical challenges for the analytical model to simulate temperature field close to the boundary in three-dimensional builds.

5. Summary and conclusions

A three-dimensional analytical heat transfer model with a volumetric heat source term is developed to predict temperature field, fusion zone dimensions and cooling rates for LPBF of multiple tracks and layers quickly and consistently. The generalized volumetric heat source term enabled the analytical model to simulate the melt pools for a range of depth to width ratio. The computed results of fusion zone dimensions were found close to the corresponding independently measured values for three commonly used alloys with diverse material properties and a wide range of LPBF process conditions. The computed values of cooling rates were also found to be fairly close to the corresponding independent experimental data.

The computational efficiency of the proposed analytical model and the contemporary numerical models was compared for small and large volumes of deposition. It was found that the proposed analytical model could simulate the temperature field for LPBF for a typical part scale build volume of 10^4 mm^3 several hundred to a thousand times faster than a contemporary numerical model. Furthermore, the analytical model could be deployed in a core i5 notebook computer with 8 GB RAM, which would be incapable to undertake numerical model calculations.

The analytically computed melt pool dimensions are further presented in the form of easy-to-use maps for different combinations of laser beam powers and scanning speeds. These maps can serve as practical guides for the selection of the suitable range of process conditions with minimal trial-and-error tests. The proposed analytical heat transfer model with its high computational efficiency has the potential to become a practical tool for the selection of parameters.

The following are the main conclusions.

- The proposed analytical heat transfer model provides realistic estimations of fusion zone dimensions along multiple tracks and layers for a range of laser beam power and scanning speeds for the three alloys studied for specimens in part scale.
- The analytically calculated cooling rates are found to be in good agreement with the corresponding independent experimental results. The estimated cooling rates can be used further to anticipate build microstructure and properties using available constitutive relations for specific alloys.
- The analytical model can consider the effect of the diverse thermophysical properties while calculating the fusion zone dimensions and cooling rates in the LPBF of commonly used alloys. The computed fusion zone dimensions at different combinations of laser power and scanning speeds are presented in the form of easy-to-use maps to help in the selection of process parameters with minimum trial-and-error tests.
- The analytical model can simulate the temperature field for the LPBF of multiple tracks and layers much faster than the available numerical models. The LPBF of a typical part scale build volume of 10^4 mm^3 could be modeled analytically only in a few tens of minutes using a core i5 notebook computer with 8 GB RAM.

Author statement

P. Zagade, B.P. Gautham, A. De, T. DebRoy: Conception and

design of study. **P. Zagade**: Acquisition of data. **P. Zagade, B.P. Gautham, A. De, T. DebRoy**: Analysis and/or interpretation of data. **P. Zagade**: Drafting the manuscript. **B.P. Gautham, A. De, T. DebRoy**: Revising the manuscript critically for important intellectual content. **P. Zagade, B.P. Gautham, A. De, T. DebRoy**: Approval of the version of the manuscript to be published.

Declaration of Competing Interest

The authors declare that they have no known competing financial interests or personal relationships that could have appeared to influence the work reported in this paper.

Appendix-I

Eq. (1) can be expressed as follows considering temperature-dependent thermal conductivity and specific heat as

$$\nabla(k(T)\nabla T) = \rho C(T)\frac{\partial T}{\partial t} - \dot{Q} \tag{A1}$$

The consideration of thermal conductivity and specific heat as a function of temperature results Eq. (1) to transform to a non-linear form and the same can be brought to a linear form by expressing the material properties in terms of a function Π such that [45],

$$k = k_0\left(\frac{\partial\Pi}{\partial T}\right) \tag{A2}$$

$$C = C_0\left(\frac{\partial\Pi}{\partial T}\right) \tag{A3}$$

where k_0 and C_0 are material constants, The function Π can be referred to "pseudo temperature functional" and is chosen such that $(\partial\Pi/\partial T)$ is a linear function of temperature as $(1+mT)$ to approximate the temperature dependent thermophysical properties [45]. Substituting Eq. (A2) and (A3) in Eq. (A1), the latter can be written as:

$$k_0\nabla^2\Pi = \rho C_0\frac{\partial\Pi}{\partial t} - \dot{Q} \tag{A4}$$

Eq. (A4) is in a linear form and the corresponding boundary and initial conditions, Eqs. (2)–(4), can be expressed in terms of Π as

$$(\Pi - \Pi_0) = 0 \text{ at } (x \to \pm\infty, \ y \to \pm\infty, \ z \to -\infty) \tag{A5}$$

$$\frac{\partial\Pi}{\partial z} = 0 \text{ at } z = 0 \tag{A6}$$

$$\Pi = \Pi_0 \text{ at } t = 0 \tag{A7}$$

where Π_0 is the initial value of Π corresponding to T_0 i.e. $\Pi(T_0)$. The solution of Eq. (A4) can be obtained using Green's function approach and the general solution for an initial condition $\Pi(x,y,z,t) = \Pi_0$ with Π_0 as a constant can be expressed as

$$\Pi(x, y, z, t) - \Pi_0$$

$$= \int_0^t \int_{-\infty}^{+\infty} \int_{-\infty}^{+\infty} \int_{-\infty}^{+\infty} \chi(x - \xi, y - \varsigma, z - \zeta, t - t')\dot{Q}(\xi, \varsigma, \zeta, t')d\xi d\varsigma d\zeta dt' \tag{A8}$$

where χ is the Green's function for three-dimensional diffusion and is given as

$$\chi(x - \xi, y - \varsigma, z - \zeta, t - t')$$

$$= \frac{1}{\{4\pi\alpha(t - t')\}^{3/2}}\exp\left\{-\frac{(x - \xi)^2 + (y - \varsigma)^2 + (z - \zeta)^2}{4\alpha(t - t')}\right\} \tag{A9}$$

The analytical solution for increment in $(\Pi - \Pi_0)$ at any location in the domain (x,y,z) in time t due to a volumetric heat source, Eq. (5), moving along the linear tracks from a starting location (x_s, y_s, z_s) with speeds v_x and v_y respectively along X and Y directions can be given as

$$\Pi - \Pi_0 = \int_{t'=0}^{t'=t} \int_{-\infty}^{+\infty} d\xi \int_{-\infty}^{+\infty} d\varsigma \int_{-\infty}^{+\infty} d\zeta \frac{f_p \eta P}{\rho C_0 \pi r_b^2 (4\pi\alpha t')^{3/2}}$$

$$\times \exp\left[-\frac{f_p\{\xi\}^2 + f_p\{\varsigma\}^2}{r_b^2}\right]\frac{\sqrt{f_d}}{h\sqrt{\pi}}\exp\left(-\frac{f_d\zeta^2}{h^2}\right) \tag{A10}$$

$$\times \exp\left\{-\frac{(x - \xi)^2 + (y - \varsigma)^2 + (z - \zeta)^2}{4\alpha t'}\right\}dt'$$

and, solving the spatial integrals for the semi-infinite boundary conditions, Eq. (A10) can be written as

$$\Pi - \Pi_0 = \int_{t'=0}^{t'=t} \frac{2f_p\eta P\sqrt{f_d}}{\rho C_0 \pi \sqrt{\pi}} \frac{1}{\tau''}$$

$$\times \exp\left\{ -\frac{f_p\{(x'')^2 + (y'')^2\}}{4f_p\alpha t'' + r_b^2} - \frac{f_d z^2}{4f_d\alpha t'' + h^2} \right\} dt' \tag{A11}$$

The terms x'', y'' and t'' are given already in Eqs. (11)–(14). The temperature field can then be calculated as

$$T(x, y, z, t)$$

$$= \frac{1}{m}\left\{ \sqrt{2m(\Pi - \Pi_0) + (1 + mT_0)^2} - 1 \right\} \tag{A12}$$

It is worthwhile to mention that using the similar method and keeping all other conditions the same, the analytical solution of the temperature field with uniform and temperature independent material properties can be given as

$$T - T_0 = \int_{t'=0}^{t'=t} \frac{2f_p\eta P\sqrt{f_d}}{\rho C \pi \sqrt{\pi}} \frac{1}{\tau''}$$

$$\times \exp\left\{ -\frac{f_p\{(x'')^2 + (y'')^2\}}{4f_p\alpha t'' + r_b^2} - \frac{f_d z^2}{4f_d\alpha t'' + h^2} \right\} dt' \tag{A13}$$

A further substitution in Eq. (A12) provides the analytical solution for the temperature field for a single linear track as presented in Eq. (10). It can be extended further to account for multiple tracks by using superposition principle applied to pseudo temperature functional and is presented in Eq. (15).

Appendix-II

The cooling rate for the deposition of a single linear track is obtained by differentiating Eq. (10) with respect to time t. Considering a laser beam starting at location (0,0,0) and moving with a constant scanning speed of v_x along the positive X-direction to form a single linear track, the cooling rate on the top surface of the melt pool can be expressed as

$$\frac{dT}{dt} =$$

$$\frac{d\varphi}{dt}\left(2m\left[\int_{t'=0}^{t'=t} \frac{2f_p\eta P\sqrt{f_d}}{\rho C_0 \pi \sqrt{\pi}} \frac{1}{\tau''} \exp\left\{ -\frac{f_p\{(x'')^2\}}{4f_p\alpha t'' + r_b^2} \right\} dt' \right] + (1 + mT_0)^2 \right)^{-0.5} \tag{A14}$$

where

$$\frac{d\varphi}{dt} = \frac{2f_p\eta P\sqrt{f_d}}{\rho C_0 \pi \sqrt{\pi}}$$

$$\times \int_0^t \frac{1}{\tau''}\left[\frac{4f_p^2\alpha(x'')^2}{\{4f_p\alpha t'' + r_b^2\}^2} - \frac{4f_p\alpha}{4f_p\alpha t'' + r_b^2} - \frac{2f_d\alpha}{4f_p\alpha t'' + h^2} \right] \tag{A15}$$

$$\times \exp\left\{ -\frac{f_p(x'')^2}{4f_p\alpha t'' + r_b^2} \right\} dt'$$

The computed values of cooling rate can be used further to estimate the microhardness, H by using a constitutive relations from independent literature [52–54].

$$H = 3\sigma_Y(0.1)^{-0.25} \tag{A16}$$

where, the yield stress σ_Y can be expressed in terms of cooling rate as

$$\sigma_Y = \sigma_0 + D \times \left\{ p \times \left(\frac{dT}{dt} \right)^{-q} \right\}^{-0.5} \tag{A17}$$

and σ_0, p, q and D are materials constants with values 240 MPa, 80, 0.33 and 279, respectively for SS316L [53,54].

References

[1] T. DebRoy, H.L. Wei, J.S. Zuback, T. Mukherjee, J.W. Elmer, J.O. Milewski, A. M. Beese, A. Wilson-Heid, A. De, W. Zhang, Additive manufacturing of metallic components – Process, structure and properties, Prog. Mater. Sci. 92 (2018) 112–224, https://doi.org/10.1016/j.pmatsci.2017.10.001.

[2] J.O. Milewski, Additive Manufacturing of Metals: From Fundamental Technology to Rocket Nozzles, Medical Implants and Custom Jewelry, Springer, Berlin Heidelberg, New York, NY, 2017.

[3] T. DebRoy, T. Mukherjee, H.L. Wei, J.W. Elmer, J.O. Milewski, Metallurgy, mechanistic models, and machine learning in metal printing, Nat. Rev. Mater. 6 (1) (2021) 48–68, https://doi.org/10.1038/s41578-020-00236-1.

[4] H.L. Wei, T. Mukherjee, W. Zhang, J.S. Zuback, G.L. Knapp, A. De, T. DebRoy, Mechanistic models for additive manufacturing of metallic components, Prog. Mater. Sci. 116 (2021), 100703, https://doi.org/10.1016/j.pmatsci.2020.100703.

[5] T. Mukherjee, H.L. Wei, A. De, T. DebRoy, Heat and fluid flow in additive manufacturing—Part I: Modeling of powder bed fusion, Comput. Mater. Sci. 150 (2018) 304–313, https://doi.org/10.1016/j.commatsci.2018.04.022.

[6] T. Mukherjee, H.L. Wei, A. De, T. DebRoy, Heat and fluid flow in additive manufacturing – Part II: powder bed fusion of stainless steel, and titanium, nickel and aluminum base alloys, Comput. Mater. Sci. 150 (2018) 369–380, https://doi.org/10.1016/j.commatsci.2018.04.027.

[7] S.A. Khairallah, A.T. Anderson, A. Rubenchik, W.E. King, Laser powder-bed fusion additive manufacturing: physics of complex melt flow and formation mechanisms of pores, spatter, and denudation zones, Acta Mater. 108 (2016) 36–45, https://doi.org/10.1016/j.actamat.2016.02.014.

[8] M. Xia, D. Gu, G. Yu, D. Dai, H. Chen, Q. Shi, Porosity evolution and its thermodynamic mechanism of randomly packed powder-bed during selective laser melting of Inconel 718 alloy, Int. J. Mach. Tools Manuf. 116 (2017) 96–106, https://doi.org/10.1016/j.ijmachtools.2017.01.005.

[9] M. Bayat, A. Thanki, S. Mohanty, A. Witvrouw, S. Yang, J. Thorborg, N.S. Tiedje, J. H. Hattel, Keyhole-induced porosities in Laser-based Powder Bed Fusion (L-PBF) of Ti6Al4V: high-fidelity modelling and experimental validation, Addit. Manuf. 30 (2019), 100835, https://doi.org/10.1016/j.addma.2019.100835.

[10] T. Mukherjee, T. DebRoy, Mitigation of lack of fusion defects in powder bed fusion additive manufacturing, J. Manuf. Process. 36 (2018) 442–449, https://doi.org/10.1016/j.jmapro.2018.10.028.

[11] V. Manvatkar, A. De, T. DebRoy, Spatial variation of melt pool geometry, peak temperature and solidification parameters during laser assisted additive manufacturing process, Mater. Sci. Technol. 31 (2015) 924–930, https://doi.org/10.1179/1743284714Y.0000000701.

[12] E.R. Denlinger, J. Irwin, P. Michaleris, Thermomechanical modeling of additive manufacturing large parts, J. Manuf. Sci. Eng. 136 (2014), 061007, https://doi.org/10.1115/1.4028669.

[13] N.E. Hodge, R.M. Ferencz, J.M. Solberg, Implementation of a thermomechanical model for the simulation of selective laser melting, Comput. Mech. 54 (2014) 33–51, https://doi.org/10.1007/s00466-014-1024-2.

[14] V. Manvatkar, A. De, T. DebRoy, Heat transfer and material flow during laser assisted multi-layer additive manufacturing, J. Appl. Phys. 116 (2014), 124905, https://doi.org/10.1063/1.4896751.

[15] A.J. Dunbar, E.R. Denlinger, M.F. Gouge, P. Michaleris, Experimental validation of finite element modeling for laser powder bed fusion deformation, Addit. Manuf. 12 (2016) 108–120, https://doi.org/10.1016/j.addma.2016.08.003.

[16] K. Khan, A. De, Modelling of selective laser melting process with adaptive remeshing, Sci. Technol. Weld. Join. 24 (2019) 391–400, https://doi.org/10.1080/13621718.2019.1575057.

[17] K. Khan, G. Mohr, K. Hilgenberg, A. De, Probing a novel heat source model and adaptive remeshing technique to simulate laser powder bed fusion with experimental validation, Comput. Mater. Sci. 181 (2020), 109752, https://doi.org/10.1016/j.commatsci.2020.109752.

[18] D. Rosenthal, The theory of moving source of heat and its application to metal transfer, Trans. ASME 43 (1946).

[19] R. Komanduri, Z.B. Hou, Thermal analysis of the arc welding process: part I. General solutions, Metall. Mater. Trans. B 31 (2000) 1353–1370, https://doi.org/10.1007/s11663-000-0022-2.

[20] A.J. Pinkerton, L. Li, The development of temperature fields and powder flow during laser direct metal deposition wall growth, J. Mech. Eng. Sci. 218 (2004) 531–541, https://doi.org/10.1243/095440604323052319.

[21] J. Winczek, Modeling of heat affected zone in multipass GMAW surfacing S235 steel element, Procedia Eng. 136 (2016) 108–113, https://doi.org/10.1016/j.proeng.2016.01.182.

[22] H.L. Wei, H.K.D.H. Bhadeshia, S.A. David, T. DebRoy, Harnessing the scientific synergy of welding and additive manufacturing, Sci. Technol. Weld. Join. 24 (2019) 361–366, https://doi.org/10.1080/13621718.2019.1615189.

[23] J.P. Oliveira, T.G. Santos, R.M. Miranda, Revisiting fundamental welding concepts to improve additive manufacturing: from theory to practice, Prog. Mater. Sci. 107 (2020), 100590, https://doi.org/10.1016/j.pmatsci.2019.100590.

[24] T. Mukherjee, V.D. Manvatkar, A. De, T. DebRoy, Dimensionless numbers in additive manufacturing, J. Appl. Phys. 121 (2017), 064904, https://doi.org/10.1063/1.4976006.

[25] E.J. Schwalbach, S.P. Donegan, M.G. Chapman, K.J. Chaput, M.A. Groeber, A discrete source model of powder bed fusion additive manufacturing thermal history, Addit. Manuf. 25 (2019) 485–498, https://doi.org/10.1016/j.addma.2018.12.004.

[26] J. Ning, D. Sievers, H. Garmestani, S. Liang, Analytical modeling of in-process temperature in powder bed additive manufacturing considering laser power

[27] P. Promoppatum, S.-C. Yao, P.C. Pistorius, A.D. Rollett, A comprehensive comparison of the analytical and numerical prediction of the thermal history and solidification microstructure of Inconel 718 products made by laser powder-bed fusion, Engineering 3 (2017) 685–694, https://doi.org/10.1016/J.ENG.2017.05.023.

[28] A. Plotkowski, M.M. Kirka, S.S. Babu, Verification and validation of a rapid heat transfer calculation methodology for transient melt pool solidification conditions in powder bed metal additive manufacturing, Addit. Manuf. 18 (2017) 256–268, https://doi.org/10.1016/j.addma.2017.10.017.

[29] R. Forslund, A. Snis, S. Larsson, Analytical solution for heat conduction due to a moving Gaussian heat flux with piecewise constant parameters, Appl. Math. Model. 66 (2019) 227–240, https://doi.org/10.1016/j.apm.2018.09.018.

[30] H.S. Carslaw, J.C. Jaeger. Conduction of Heat in Solids, 2nd ed., Oxford Science Publications, 1986.

[31] A.V. Gusarov, J.-P. Kruth, Modelling of radiation transfer in metallic powders at laser treatment, Int. J. Heat Mass Transf. 48 (2005) 3423–3434, https://doi.org/10.1016/j.ijheatmasstransfer.2005.01.044.

[32] N.T. Nguyen, A. Ohta, K. Matsuoka, N. Suzuki, Y. Maeda, Analytical solutions for transient temperature of semi-infinite body subjected to 3-D moving heat sources, Weld. Res. (1999) 10.

[33] W.E. King, H.D. Barth, V.M. Castillo, G.F. Gallegos, J.W. Gibbs, D.E. Hahn, C. Kamath, A. Rubenchik, Observation of keyhole-mode laser melting in laser powder-bed fusion additive manufacturing, J. Mater. Process. Technol. 214 (2014) 2915–2925, https://doi.org/10.1016/j.jmatprotec.2014.06.005.

[34] J.J.S. Dilip, S. Zhang, C. Teng, K. Zeng, C. Robinson, D. Pal, B. Stucker, Influence of processing parameters on the evolution of melt pool, porosity, and microstructures in Ti-6Al-4V alloy parts fabricated by selective laser melting, Prog. Addit. Manuf. 2 (2017) 157–167, https://doi.org/10.1007/s40964-017-0030-2.

[35] S. Patel, M. Vlasea, Melting modes in laser powder bed fusion, Materialia 9 (2020), 100591, https://doi.org/10.1016/j.mtla.2020.100591.

[36] Y. Wang, C. Kamath, T. Voisin, Z. Li, A processing diagram for high-density Ti-6Al-4V by selective laser melting, Rapid Prototyp. J. 24 (2018) 1469–1478, https://doi.org/10.1108/RPJ-11-2017-0228.

[37] R. Cunningham, C. Zhao, N. Parab, C. Kantzos, J. Pauza, K. Fezzaa, T. Sun, A. D. Rollett, Keyhole threshold and morphology in laser melting revealed by ultrahigh-speed x-ray imaging, Science 363 (2019) 849–852, https://doi.org/10.1126/science.aav4687.

[38] A.M. Philo, S. Mehrabian, M. Holmes, S. Sillars, C.J. Sutcliffe, J. Sienz, S.G. R. Brown, N.P. Lavery, A pragmatic continuum level model for the prediction of the onset of keyholing in laser powder bed fusion, Int. J. Adv. Manuf. Technol. 101 (2019) 697–714, https://doi.org/10.1007/s00170-018-2770-7.

[39] U. Scipioni Bertoli, A.J. Wolfer, M.J. Matthews, J.-P.R. Delplanque, J. M. Schoenung, On the limitations of volumetric energy density as a design parameter for selective laser melting, Mater. Des. 113 (2017) 331–340, https://doi.org/10.1016/j.matdes.2016.10.037.

[40] C. Kamath, Data mining and statistical inference in selective laser melting, Int. J. Adv. Manuf. Technol. 86 (2016) 1659–1677, https://doi.org/10.1007/s00170-015-8289-2.

[41] H. Hyer, L. Zhou, S. Park, G. Gottsfritz, G. Benson, B. Tolentino, B. McWilliams, K. Cho, Y. Sohn, Understanding the Laser Powder Bed Fusion of AlSi10Mg Alloy, Metallogr. Microstruct. Anal. 9 (2020) 484–502, https://doi.org/10.1007/s13632-020-00659-w.

[42] K.C. Mills, Recommended Values of Thermophysical Properties for Selected Commercial Alloys, Woodhead Publishing, Cambridge, 2002.

[43] M. Van Elsen, M. Baelmans, P. Mercelis, J.-P. Kruth, Solutions for modelling moving heat sources in a semi-infinite medium and applications to laser material processing, Int. J. Heat Mass Transf. 50 (2007) 4872–4882, https://doi.org/10.1016/j.ijheatmasstransfer.2007.02.044.

[44] R. Rai, J.W. Elmer, T.A. Palmer, T. DebRoy, Heat transfer and fluid flow during keyhole mode laser welding of tantalum, Ti–6Al–4V, 304L stainless steel and vanadium, J. Phys. Appl. Phys. 40 (2007) 5753–5766, https://doi.org/10.1088/0022-3727/40/18/037.

[45] R.J. Grosh, E.A. Trabant, G.A. Hawkins, Temperature distribution in solids of variable thermal properties heated by moving heat sources, Q. Appl. Math. 13 (1955) 161–167, https://doi.org/10.1090/qam/72360.

[46] Z. Dong, Y. Liu, W. Wen, J. Ge, J. Liang, Effect of hatch spacing on melt pool and as-built quality during selective laser melting of stainless steel: modeling and experimental approaches, Materials 12 (2018) 50, https://doi.org/10.3390/ma12010050.

[47] U. Scipioni Bertoli, G. Guss, S. Wu, M.J. Matthews, J.M. Schoenung, In-situ characterization of laser-powder interaction and cooling rates through high-speed imaging of powder bed fusion additive manufacturing, Mater. Des. 135 (2017) 385–396, https://doi.org/10.1016/j.matdes.2017.09.044.

[48] M. Ma, Z. Wang, X. Zeng, A comparison on metallurgical behaviors of 316L stainless steel by selective laser melting and laser cladding deposition, Mater. Sci. Eng. A 685 (2017) 265–273, https://doi.org/10.1016/j.msea.2016.12.112.

[49] M.J. Ansari, D.-S. Nguyen, H.S. Park, Investigation of SLM process in terms of temperature distribution and melting pool size: modeling and experimental approaches, Materials 12 (2019) 1272, https://doi.org/10.3390/ma12081272.

[50] R.J. Williams, C.M. Davies, P.A. Hooper, A pragmatic part scale model for residual stress and distortion prediction in powder bed fusion, Addit. Manuf. 22 (2018) 416–425, https://doi.org/10.1016/j.addma.2018.05.038.

absorption, latent heat, scanning strategy, and powder packing, Materials 12 (2019) 808–815, https://doi.org/10.3390/ma12050808.

[51] Y.S. Lee, W. Zhang, Modeling of heat transfer, fluid flow and solidification microstructure of nickel-base superalloy fabricated by laser powder bed fusion, Addit. Manuf. 12 (2016) 178–188, https://doi.org/10.1016/j.addma.2016.05.003.

[52] H. Matyja, B.C. Giessen, N.J. Grant, The effect of cooling rate on the dendrite spacing in splat-cooled aluminium alloys, J. Inst. Metal 96 (1968) 30–32.

[53] J.W. Elmer, S.M. Allen, T.W. Eagar, Microstructural development during solidification of stainless steel alloys, Metall. Trans. A. 20 (1989) 2117–2131, https://doi.org/10.1007/BF02650298.

[54] B.P. Kashyap, K. Tangri, On the Hall-Petch relationship and substructural evolution in type 316L stainless steel, Acta Metall. Mater. 43 (1995) 3971–3981, https://doi.org/10.1016/0956-7151(95)00110-H.

[55] T. DebRoy, H.K.D.H. Bhadeshia, Innovations in Everyday Engineering Materials, Springer, 2021, pp. 59–60, https://doi.org/10.1007/978-3-030-57612-7_5.

[56] L.E. Svensson, B. Gretoft, H.K.D.H. Bhadeshia, An analysis of cooling curves from the fusion zone of steel weld deposits, Scand. J. Metall. 15 (1986) 97–103.